# Raman mapping analysis for removal of surface secondary phases of CZTS films using chemical etching

Zhengfei Wei, [a] Michael J. Newman, Wing C. Tsoi, and Trystan M. Watson [a]

[1]*SPECIFIC, College of Engineering, Swansea University, Engineering East, Bay Campus, Swansea, SA1 8EN*

Raman spectroscopy has been widely used as a non-destructive surface characterization method for the $Cu_2ZnSnS_4$ (CZTS) thin films. Secondary phases, which often co-exist with CZTS, are detrimental to the device performance. In this work, removal of the secondary phases using sodium sulfide ($Na_2S$) aqueous solution etching in various time durations was investigated. Raman scattering mapping provides a direct visualization of phase distribution in CZTS-based materials on a relatively large scale (1mm × 10 mm). Both as-grown and etched CZTS absorber layers were examined by Raman spectroscopy with a 532 nm excitation laser light in the range of 50 to 500 $cm^{-1}$. A clear reduction of the secondary phases (mainly SnS) at the surface after etching was confirmed by Raman and scanning electron microscope (SEM). Room temperature photoluminescence (PL) reveals a pronounced correlation between the amount of secondary phases and photoluminescence peak position. The PL spectra of the regions with more Sn-rich secondary phases show clearly a shift to high wavelength of the peak position, in comparison with regions with less Sn-rich secondary phases. These observed PL changes could be due to Sn-rich defects which may cause recombination processes.

Earth abundant element based $Cu_2ZnSn(S,Se)_4$ (CZTSSe) absorber material has shown great potential as an alternative to industrial-proven $Cu(In,Ga)Se_2$ solar cells. The power conversion efficiency of CZTSSe-based solar cell has reached to 12.7% in 2014,[1] but there is room for improvement to compete with 22.3% record device in $Cu(In,Ga)Se_2$ (CIGS) technologies.[2] Several physical mechanisms have been proposed to explain this efficiency gap including interface losses, electrostatic potential fluctuation or bandgap fluctuation, and defects driven recombination.[3-5] The existence of secondary phase materials at the pn-junction interface could lead to one or more of the above energy loss mechanisms. Secondary phases such as $Cu_2SnS_3$ or SnS having a low-bandgap at the interface can cause a decrease in open circuit voltage, while ZnS with high-bandgap can act as a photocurrent barrier and is usually responsible for a high series resistance.[5] Binary copper phases have high conductivity and

[a] Authors to whom correspondence should be addressed. Electronic mail: Zhengfei.Wei@swansea.ac.uk and T.M.Watson@swansea.ac.uk.

normally result in shunted device.[6] Chemical etching is a simple and effective method for removal of these detrimental secondary phases. Bromine in a methanol solution ($Br_2$/MeOH) has been reported to etch $Cu_2SnS_3$ effectively.[7] The use of HCl solution at 75 °C has been proved to be efficient in removing ZnS.[8] KCN etching is the most common method for CZTSSe and CIGS processing to remove Cu-S and Cu-Se.[6] Removing SnS is less reported, which may be due to most of CZTS preparation processes leading to a Sn-loss in the final film.[9] Xie *et al.* found a chemical route using $(NH_4)_2S$ to successfully remove Sn(S,Se).[10]

Raman spectroscopy is a powerful technique to identify a number of CZTS and secondary phases at the surface, which could provide essential feedback for the optimization of process parameters and film growth.[11] Raman mapping is used to rapidly gather comprehensive 2D distribution of crystalline phases, which could play a significant role in monitoring absorber film quality during industrial production.[12] In our recent work, we demonstrated to use a sulfur-rich precursor to reduce sulfur-loss in the high temperature annealing process.[13] However, a SnS secondary phase was repeatedly found at the CZTS surface using sulfur-rich precursor solution. We now show aqueous $Na_2S$ solution could effectively remove these SnS surface impurities, which was confirmed by using Raman spectroscopy and SEM. The ratio of impurity/CZTS data collected from the Raman mapping was used to illustrate phase distribution on a selected representative large area (1 mm × 10 mm). Comparing single-peak intensity mapping, the ratio mapping was selected because it can give the much better resolution on SnS distribution.

In this work, 1.7 μm thick CZTS layers were grown on Mo coated soda-lime glass substrates by spin-coating of C-Z-T-S solution precursors and subsequently sulfurized in a rapid thermal processing (RTP) furnace at 550 °C for 20 mins. The preparation details can be found in Ref. 13. After sulfurization, the sample *A* was cut into three identical pieces. One piece of CZTS sample (sample *A*) after cutting was shown in Figure 1. Thus, two pieces (sample *B* and *C*) were chemically etched in a 1M

$Na_2S$ aqueous solution for 30 s and 60 s, respectively. X-ray diffraction (XRD) (not shown) shows almost no difference on the spectra of these three samples, which means three samples have similar crystalline phases in the bulk. To identify the surface phase distribution, SEM and Raman spectroscopy were performed with a Renishaw inVia Raman microscope using a laser with an excitation wavelength of 532 nm (~3mW) on a spot with a diameter around 1 μm. Raman mapping was performed with a motorized scanning stage which enables a 1 mm × 10 mm scanning area (Figure 1) using a line-focus laser. All the Raman maps had a pixel size of 32.5 μm × 32.5 μm for both *x* and *y* direction. The spectral resolution is 1 $cm^{-1}$. The intensity of a Raman peak was extracted from the maximum value after baseline subtraction using Gaussian curve fitting over corresponding spectral range (123-210 $cm^{-1}$ for SnS and 313-336 $cm^{-1}$ for *A* mode of CZTS).[14] Thus, $\frac{I_{SnS}}{I_{CZTS}}$ ratio map was created to present the resolved secondary distribution and relative portion of the secondary phase, where $I_{SnS}$ represents the background corrected intensity of SnS peaks at 158 $cm^{-1}$, 183 $cm^{-1}$, and 222 $cm^{-1}$; and $I_{CZTS}$ represents the background corrected intensity of CZTS peak at 338 $cm^{-1}$. The curve fitting and background subtraction were processed using Renishaw WiRE 4.1 software package. All the SnS and CZTS peaks were fitted with Gaussian curves. Then, the intensity of SnS and CZTS peaks was exacted from fitted curves. Room temperature photoluminescence measurements were performed using the same Raman system and the same laser wavelength. When performing the PL measurements, the 1800 lines/mm grating for Raman measurement was switched to a 300 lines/mm grating which allows the detection of a certain range of wavelengths for PL. Three locations (marked as Center, Quarter and Edge in Figure 1) on the Raman mapping area were selected to investigate the effect of the surface impurities on CZTS using both Raman and PL.

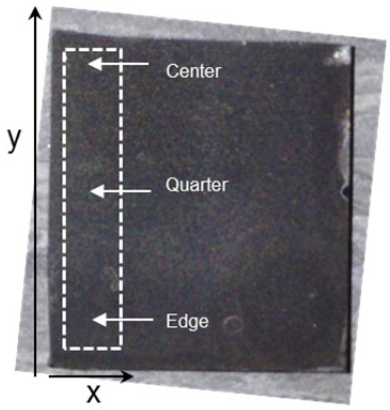


FIG. 1. A photo of one piece of CZTS thin film sample after cutting. The Raman mapping area was marked as dotted rectangular. Three representative locations were labeled as Center, Quarter, and Edge corresponding to the selected measurement regions. x and y represent the scanning directions of Raman mapping.

Raman mapping on the CZTS samples are shown in Figures 2A1 for as-grown sample, 2B1 for sample after $Na_2S$ etching for 30 s, and 2C1 for sample after $Na_2S$ etching for 60 s, respectively. In Figure 2A1, a sharp reduction of $\frac{I_{SnS}}{I_{CZTS}}$ ratio for the as-grown sample from the Center (1.3) to the Edge (0.1) represents a pronounced SnS coverage at the Center part of the CZTS surface. Most dominant red regions in Figure 2A1 (Center of sample *A*) and a few red spots show the existence of SnS. This is confirmed by the two individual spectra collected at the center and at the edge of the mapped sample as shown in Figure 2A2. Three peaks at 158 $cm^{-1}$, 183 $cm^{-1}$, and 222 $cm^{-1}$ can be assigned to SnS,[14] which could be correlated with the fine semicircular grains (with a better observation in Figure 2A4) or large disk shape grains for typical SnS grains embedded in CZTS grains in Figure 2A3.[10] The $\frac{I_{SnS}}{I_{CZTS}}$ ratio map of sample *B* which is after etching in $Na_2S$ for 30 s in Figure 2B1. Remarkably, $\frac{I_{SnS}}{I_{CZTS}}$ ratios are in the range of 0 - 1 over most the area of sample *B* which means the significant reduction of SnS phases, with the notable exception of a few isolated red spots displaying relatively high $\frac{I_{SnS}}{I_{CZTS}}$ ratio. These residual

SnS phases (red spots) could indicate a longer etching time required to remove all these impurities. Furthermore, the drop of the intensity of three SnS peaks from spectrum taken from the Center location of sample *B* suggests pronounced removal of SnS from CZTS surface in Figure 2B2. However, there are still small semicircular shape grains embedded on the CZTS as shown in SEM image (Figure 2B3) indicating the existence of SnS. After etching in $Na_2S$ for 60 s, $\frac{I_{SnS}}{I_{CZTS}}$ ratios reduced to 0-0.5 for nearly the whole area of sample *C* in Figure 2C1. Although no red spots found in the whole $\frac{I_{SnS}}{I_{CZTS}}$ mapping area, more light green spots ($\frac{I_{SnS}}{I_{CZTS}}$ ~0.5) appear in sample *C* (Figure 2C1) than in sample *B* (Figure 2B1). We suggest that some of CZTS could be removed by $Na_2S$ etching as well to cause the increase $\frac{I_{SnS}}{I_{CZTS}}$ ratios in the Center (more cyan color appeared). In Figure 2C2, the Raman spectra taken from the center part of sample *C* shows the similar intensity of SnS compared with sample *B* (Figure 2B2). However, more blue points appeared in the center part of sample *C* (Figure 2C1) than sample *A* (Figure 2A1) and sample *B* (Figure 2B1). The effective removal of SnS can be also evident from few of semicircular grains on the CZTS surface in SEM images shown in Figure 2C3.

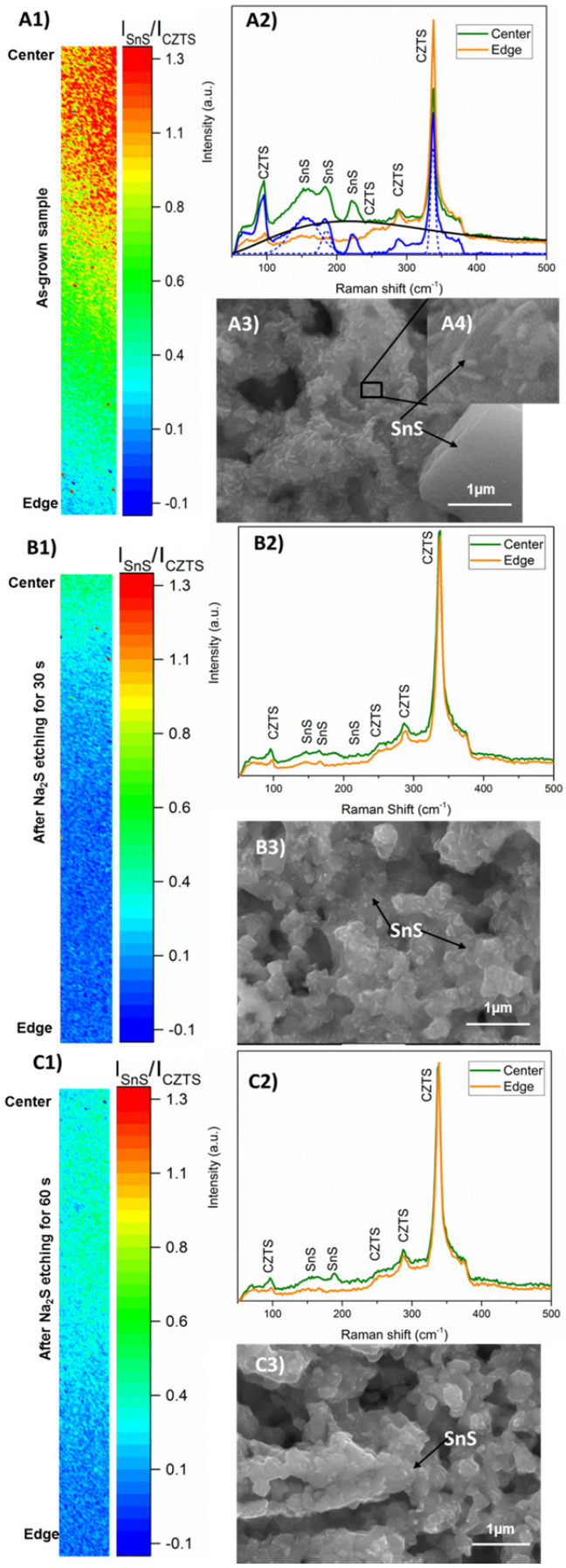
A1)
$I_{SnS}/I_{CZTS}$
Center
Edge
As-grown sample
1.3
1.1
0.8
0.6
0.4
0.1
-0.1
A2)
Center
Edge
CZTS
SnS
Intensity (a.u.)
Raman shift ($cm^{-1}$)
100
200
300
400
500
A3)
A4)
SnS
1μm
B1)
After $Na_2S$ etching for 30 s
B2)
Raman Shift ($cm^{-1}$)
B3)
C1)
After $Na_2S$ etching for 60 s
C2)
C3)

FIG. 2. Raman spectroscopic mapping of CZTS samples on a 1 mm × 10 mm (*x*-*y*) region. (A1), (B1), and (C1) $\frac{I_{SnS}}{I_{CZTS}}$ intensity ratio map of SnS/CZTS for sample *A*, *B*, and *C,* respectively. (A2), (B2), and (C2) Two individual Raman spectra taken form two representative locations (labeled as Center and Edge) from the mapped CZTS sample *A*, *B*, and *C*, respectively. (A3), (B3), and (C3) SEM images of the center location of the CZTS sample *A, B, and C,* respectively. (A4) The inserted image of the enlarged square region in (A3). The representatively subtracted background (black curve), deconvoluted curve (blue curve) and fitted Gaussian curves (dash blue curves) were plotted into the spectrum of Centre of as-grown sample in (A2) to show data processing procedure of mapping data.

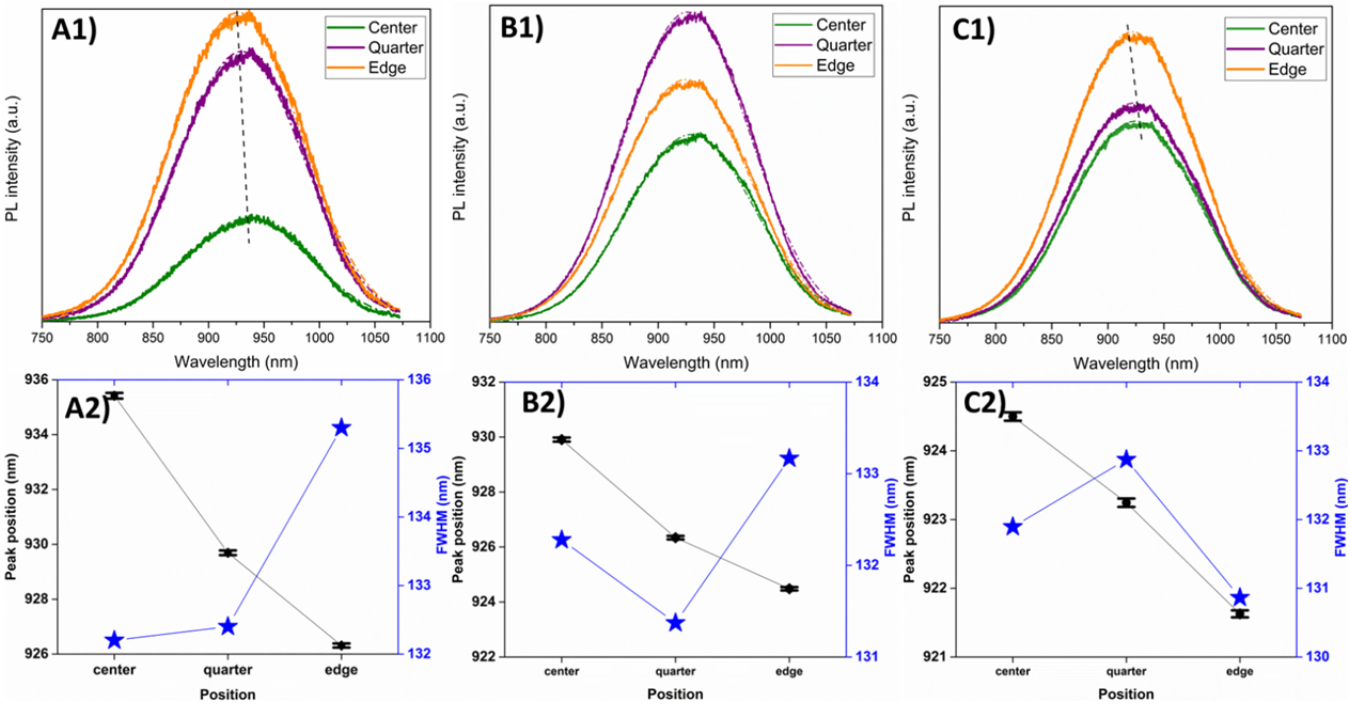


FIG. 3. PL analysis of three individual locations (labelled as Center, Quarter and Edge) CZTS samples *A*, *B,* and *C* on a 1 mm × 10 mm (*x*-*y*) region. (A1), (B1), and (C1) The experimental PL spectra (solid lines) with Gaussian fitting curves (dotted line) of CZTS sample *A, B*, and *C,* respectively. (A2), (B2) and (C2) Peak positions (black dots with error bars) and FWHMs (blue stars) of PL spectra extracted from Gaussian fitting curves of CZTS sample *A, B, and C,* respectively.

PL spectra were collected from three representative locations (Center, Quarter, and Edge) at the same positions where Raman spectra measured of as-grown CZTS sample, CZTS sample etched in $Na_2S$ for 30 s, and CZTS sample etched in $Na_2S$ for 60 s. In Figure 3A1, there is clear blue shift of PL spectra from Sn-rich Center location to Sn-poor Edge location for as-grown CZTS sample *A*, accompanied by an incensement of PL intensity. All the spectra were fitted with Gaussian curves to extract useful parameters such as peak position and full width half maximum (FWHM). It was estimated that a small shift (~10 nm) from the Center position to the Edge position (with low concentration of SnS phases). The similar Sn-related blue shift of CZTS PL peaks has been reported in Ref. 15. For most of high performance CZTS devices with Cu-poor and Zn-rich composition (Sn-rich), the excess Sn would form point defects such as $Sn_{Cu}$ and $Sn_{Zn}$ antisites, or neutral defect complexes such as $(2Cu_{Zn} + Sn_{Zn})$.[15, 16] These defects are most likely to result in deep-level recombination centers further reducing the performance of the solar cells. FWHMs of three locations vary within 4 nm for this as-grown sample. The sharp drop of PL intensity towards Sn-rich Center could indicate the Sn-related point defects.[15] The peak positions of spectra for both sample *B* (Figure 3B1) and sample *C* (Figure 3C1) show blue shifts from Sn-rich Center to Sn-poor Edge. This Sn-related peak shift of PL spectra could also possibly be caused by the light absorption of low-bandgap energy of SnS. A marginal change of FWHMs of spectra of sample *B* and sample *C* is within 2 nm (Figure 3B2 and 3C2). The variation of PL intensity of sample *B* varies differently as compared to sample *A* and sample *C*. This could be caused by the focus problem across the whole measured area or a locally non-uniform surface in the Quarter of sample B. For sample *C*, the peak shift of three spectra shows a same blue-shift toward Sn-poor region (Figure 3C1) as sample *A* (Figure 3A1).

In summary, Raman scattering mapping was shown to be a useful tool to track surface secondary phases in CZTS films, allowing identification of the significant changes triggered by chemical etching for removing undesired secondary phases in large mapping area. In addition, room temperature PL

reveals the effect of the amount of secondary phases on photoluminescence peak position of CZTS. These results enable us to quickly determine the best etching parameter and further help us to apply the most suitable etching in device fabrication of CZTS solar cells. Future studies will focus on exploring the links between Raman-mapping result and solar cell-performance in CZTS solar cells.

This work was funded by Engineering and Science Research Council (EPSRC): EP/L017792/1: Photovoltaic Technology Based on Earth-Abundant materials (PVTeam). Gabriela Kissling, Mako Ng and Laurence Peter at Bath University are acknowledged for helpful discussions on chemical etching. The authors would like to acknowledge Welsh Assembly Government funded Sêr Cyrmru Solar Project, and the M2A funding from the European Social Fund through the Welsh Government, and Renishaw plc.

1. J. Kim, H. Hiroi, T. K. Todorov, O. Gunawan, M. Kuwahara, T. Gokmen, D. Nair, M. Hopstaken, B. Shin, Y. S. Lee, W. Wang, H. Sugimoto and D. B. Mitzi, Advanced Materials **26** (44), 7427-7431 (2014).
2. See http://www.solar-frontier.com/eng/news/2015/C051171.html, for "Solar Frontier Achieves World Record Thin-Film Solar Cell Efficiency: 22.3%" (last accessed June 1, 2016).
3. S. Bourdais, C. Choné, B. Delatouche, A. Jacob, G. Larramona, C. Moisan, A. Lafond, F. Donatini, G. Rey, S. Siebentritt, A. Walsh and G. Dennler, Advanced Energy Materials, n/a-n/a (2016).
4. S. Siebentritt and S. Schorr, Progress in Photovoltaics: Research and Applications **20** (5), 512-519 (2012).
5. D. M. B. a. P. J. Dale, in *Copper Zinc Tin Sulfide-Based Thin Film Solar Cells*, edited by K. Ito (John Wiley & Sons. Ltd, 2015), pp. 107-132.
6. S. Niki, P. J. Fons, A. Yamada, Y. Lacroix, H. Shibata, H. Oyanagi, M. Nishitani, T. Negami and T. Wada, Applied Physics Letters **74** (11), 1630-1632 (1999).
7. S. López-Marino, Y. Sánchez, M. Placidi, A. Fairbrother, M. Espindola-Rodríguez, X. Fontané, V. Izquierdo-Roca, J. López-García, L. Calvo-Barrio, A. Pérez-Rodríguez and E. Saucedo, Chemistry – A European Journal **19** (44), 14814-14822 (2013).
8. A. Fairbrother, E. García-Hemme, V. Izquierdo-Roca, X. Fontané, F. A. Pulgarín-Agudelo, O. Vigil-Galán, A. Pérez-Rodríguez and E. Saucedo, Journal of the American Chemical Society **134** (19), 8018-8021 (2012).
9. A. Weber, R. Mainz and H. W. Schock, Journal of Applied Physics **107** (1), 013516 (2010).
10. H. Xie, Y. Sánchez, S. López-Marino, M. Espíndola-Rodríguez, M. Neuschitzer, D. Sylla, A. Fairbrother, V. Izquierdo-Roca, A. Pérez-Rodríguez and E. Saucedo, ACS Applied Materials & Interfaces **6** (15), 12744-12751 (2014).
11. M. Guc, S. Levcenko, I. V. Bodnar, V. Izquierdo-Roca, X. Fontane, L. V. Volkova, E. Arushanov and A. Pérez-Rodríguez, Scientific Reports **6**, 19414 (2016).
12. A.-J. Cheng, M. Manno, A. Khare, C. Leighton, S. A. Campbell and E. S. Aydil, Journal of Vacuum Science & Technology A **29** (5), 051203 (2011).

13. Z. Wei, M. Zhu, J. D. McGettrick, G. P. Kissling, L. M. Peter and T. M. Watson, MRS Advances **FirstView**, 1-6 (2016).
14. P. A. Fernandes, P. M. P. Salomé and A. F. da Cunha, Journal of Alloys and Compounds **509** (28), 7600-7606 (2011).
15. H. Du, F. Yan, M. Young, B. To, C.-S. Jiang, P. Dippo, D. Kuciauskas, Z. Chi, E. A. Lund, C. Hancock, W. M. Hlaing OO, M. A. Scarpulla and G. Teeter, Journal of Applied Physics **115** (17), 173502 (2014).
16. S. Chen, A. Walsh, X.-G. Gong and S.-H. Wei, Advanced Materials **25** (11), 1522-1539 (2013).